PERGAMON International Journal of Solids and Structures 36 (1999) 643–668

INTERNATIONAL JOURNAL OF SOLIDS and STRUCTURES

A numerical axisymmetric collapse analysis of viscoplastic cylindrical shells under axial compression

Lars Pilgaard Mikkelsen*

Department of Solid Mechanics, Technical University of Denmark, DK-2800 Lyngby, Denmark

Received 22 December 1996; in revised form 6 January 1998

Abstract

Circular cylindrical shells are frequently used as structural components because of their high strength and their ability to absorb energy during complete structural collapse. Total collapse analyses have mainly been based on experimental work and approaches inspired by this. However, in the last few years, powerful numerical tools have been available and numerical collapse analyses have become more attractive. This paper presents results from an axisymmetric numerical collapse analysis. The analysis is based on a finite rotation shell theory accounting for contact between the shell walls. The strains are assumed to remain small and the shell material is described by an elastic–viscoplastic model. The sensitivity of the collapse behaviour is demonstrated with respect to parameters such as initial imperfections, thickness of the shell, material parameters and rate of deformation. Comparisons between the results numerically obtained and approaches found in the literature are presented. Good agreement was found for the folding length of the developed collapse pattern whereas small differences between the mean crushing loads was observed. Furthermore, it was noted that the developed collapse pattern was strongly dependent on the strain hardening of the material.

Notation

List of the most important symbols. The number in brackets refers to the equation where the variable was defined or first introduced.

$(\dot{})$ time derivative
$(^{+})$ increment $(^{+}) = (\dot{})\Delta t$
$(^{\circ})$ undeformed state (Section 3)
$()_{|\alpha}$ covariant differentiation (10)
$(\bar{})$ variables to the time $t+\Delta t$ (A.1)
$\mathscr{L}^{ijkl}$ elastic moduli (6)

* Fax: 441223332662.

0020-7683/99/$ - see front matter
PII: S0020-7683(98)00026-2

l_c critical half-wave length (time-independent bifurcation analysis) (24)
l_i length of the undeformed middle surface for one half wave
l_f average length of the undeformed middle surface for one half fold
l_f^{Al} half folding length found by Alexander (1960) (25)
l_f^{AJ} half folding length found by Abramowicz and Jones (1984) (26)
l_f^{SER} half folding length found by Singace, Elsobky and Reddy (1995) (27)
E Young's modulus (3)
F middle surface (Section 3)
L length of the shell
L_d axial length of one fully developed fold
$M^{\alpha\beta}$ moment tensor (14)
$N^{\alpha\beta}$ membrane strain tensor (14)
R radius of the shell
$\mathbf{a}_i$ base vectors
$a_{\alpha\beta}$, a metric tensor of the middle surface of the shell and its determinant
$b_{\alpha\beta}$ curvature tensor of the middle surface of the shell
g^{ij} metric tensor
h thickness of the shell (14)
m rate-hardening exponent (2)
n strain hardening exponent (3)
r smallest radius of curvature of the deformed shell
s^{ij} stress deviator (2)
$\mathbf{v}$, v_i displacement vector and its components (11)
$\mathbf{w}$ difference vector (12)

Greek symbols
ΔL shortening of the shell
Δt time increment
$\alpha_{\alpha\beta}$ membrane strain tensor (8)
β degree of localisation (24)
$\bar{\xi}$ imperfection amplitude (24)
δ_α^ϱ Kronecker's delta
$\dot{\varepsilon}_0$ positive reference strain rate (2)
$\dot{\varepsilon}_L$ average shortening strain rate
ε_e^P effective plastic strain (2)
$\dot{\eta}_{ij}$ total strain rate
$\dot{\eta}_{ij}^E$, $\dot{\eta}_{ij}^P$ elastic and plastic part of strain rate
λ instantaneous load carrying capacity
λ_0 load parameter $\lambda_0 = 2\pi hR\sigma_0$
λ_{cp} load parameter $\lambda_{cp} = 2\pi hR\sigma_{cp}$
λ_m mean load carrying capacity in the near periodic region
λ_m^{Al} mean carrying capacity found by Alexander (1960) (25)
λ_m^{AJ} mean carrying capacity found by Abramowicz and Jones (1984) (26)
λ_m^{SER} mean carrying capacity found by Singace et al. (1995) (27)

λ_{max} maximum load peak
Θ^i convected coordinate system
v Poisson's ratio (6)
σ_0 reference stress (3)
σ_{cp} average axisymmetric plastic bifurcation stress
σ_e effective von Mises stress (2)
$\phi_{\alpha i}$ deformation gradients (10)
$\omega_{\alpha\beta}$ bending strain tensor (9)

1. Introduction

Buckling and initial post-buckling behaviour of circular cylindrical shells under axial compression has been the subject of intensive work for many years, experimentally as well as numerically. This is mainly due to the fact that the load carrying capacity of cylindrical shells is high, but very imperfection-sensitive. The use of thin shells as structural components is thus advantageous in places where a high strength to weight ratio is required. However, it requires extensive knowledge about imperfections. Areas in which thin-walled shell structures can be used to advantage are the automotive, aircraft and offshore industry. Both the load carrying capacity of the shell structure and the ability to absorb energy during complete structural collapse are of interest. Low peak loads and high energy absorption during total collapse are often the criteria used in estimating the crashworthiness of a shell structure. Contrary to a buckling and initial post-buckling analysis (Tvergaard, 1983a, b; Mikkelsen, 1995), a total collapse analysis requires a finite rotation shell theory that can account for contact between the shell walls. Due to the complexity of crushing problems, collapse analyses have mainly been based on experimental results (Batterman, 1965; Horton et al., 1966; Andrews et al., 1983; Singace and Elsobky, 1996; Allan, 1968) and approaches inspired thereby (Alexander, 1960; Abramowicz and Jones, 1984; Grzebieta, 1990; Wierzbicki, et al., 1992; Gupta and Velmurugan, 1995; Singace et al., 1995). With faster and larger computers, numerical analyses have become more attractive (Berstad et al., 1995) because full-scale collapse testing is costly and time consuming and the analytical approaches have limited value. Experimental measurements (Krempl and Kallianpur, 1984) show that even at a low strain rate, the inelastic behaviour of metals tends to be viscoplastic because the flow stress is dependent on the strain rate. This may have an important influence on the value of the peak load carried in the early stage of buckling and on the energy absorption during post-buckling of cylindrical shells (Mikkelsen, 1993).

For the time-independent case, a circular cylindrical shell compressed into the plastic region will bifurcate into first an axisymmetric mode and then, for sufficiently thin-walled shells, into a non-axisymmetric buckling mode, as has been shown by Tvergaard (1983a, b). These modes are initially periodic but will, after the maximum load carrying capacity of the shells is reached, localise into one buckle with a resulting rapid drop in the carrying capacity of the shell. If the non-axisymmetric bifurcation point first appears well beyond the maximum load point, such that the axisymmetric buckle has grown sufficiently large, the non-axisymmetric part will not be significant in the final buckling mode. Thus, the final collapse mode will be purely axisymmetric. It has been shown by Tvergaard (1983b) that the delay of the non-axisymmetric bifurcation point depends mainly on

the radius to thickness ratio of the shell and on the yield stress and strain hardening of the shell materials.

In the time-dependent viscoplastic case, the inelastic bifurcation point vanishes (Obrecht, 1977). The inelastic buckling behaviour is now governed by a strong sensitivity to small initial imperfections (Tvergaard, 1985). This sensitivity results in a behaviour very similar to that of the time-independent plastic shell, and the axisymmetric collapse form is also in the viscoplastic case favoured by a smaller radius to thickness ratio, a low reference stress and a low strain hardening (Mikkelsen, 1995). In the present axisymmetric analysis a preliminary assumption of a concertina collapse mode is necessary. Therefore, in all the numerical results presented, the material and geometric parameters must be chosen such that an assumption of a pure concertina collapse mode is reasonable.

The viscoplastic constitutive law (Tvergaard, 1985; Mikkelsen, 1995) used in this paper coincides with the J_2-flow theory in the time-independent limit. The analysis is performed using an incremental finite element method based on a finite rotation shell theory (Başar and Ding, 1990). In the analysis, large rotations and contact between shell walls are taken into account. The shell deformations are assumed to satisfy small strain theory, and the deformation rates are assumed small enough for inertia effects as well as effects of temperature increase due to plastic dissipation to be neglected. Special attention is devoted to the dependence of the shape of the developed axisymmetric collapse folds, of the peak loads, and of the energy absorption, with respect to the shell thickness and material parameters. By introducing a large initial localised axisymmetric imperfection (bulge) in the shell, it is demonstrated how the load peak during the initial buckling can be reduced significantly, while the energy absorption of the shell during total collapse remains almost unchanged.

Most previous analyses of total collapse of shells (e.g. Alexander, 1960; Abramowicz and Jones, 1984; Singace et al., 1995) have been based on approximate methods using rigid-plastic upper bound analysis. An important difference from these investigations is that the present numerical analysis is based on full nonlinear shell theory, accounting for large rotations. Comparisons with predictions of some of the approximate grid-plastic models are given in Section 6.

2. Elastic–viscoplastic constitutive law

In the elastic–viscoplastic model considered, it is assumed that the condition for small strain theory is satisfied and that the material hardens isotropically. The material model is identical to the model used in e.g. Tvergaard (1985), and Mikkelsen (1993, 1995), and will only be presented briefly. General tensor notation is used, where upper and lower indices denote contravariant and covariant tensors, respectively, and where the summation convention is adopted for repeated indices. Differentiation with respect to time is denoted $(\dot{\ })$, while covariant differentiation is denoted $()_{|i}$. Latin indices range from one to three, and Greek indices range from one to two.

The total strain rate $\dot{\eta}_{ij}$ is taken to be a sum of an elastic part $\dot{\eta}^{\mathrm{E}}_{ij}$ and a viscoplastic part $\dot{\eta}^{\mathrm{P}}_{ij}$

$$\dot{\eta}_{ij} = \dot{\eta}^{\mathrm{E}}_{ij} + \dot{\eta}^{\mathrm{P}}_{ij} \tag{1}$$

The elastic part is given by Hooke's law, while the viscoplastic part is modelled as

$$\dot{\eta}^{\mathrm{P}}_{ij} = \dot{\varepsilon}^{\mathrm{P}}_{\mathrm{e}} \left(\frac{3 s_{ij}}{2 \sigma_{\mathrm{e}}} \right), \quad \dot{\varepsilon}^{\mathrm{P}}_{\mathrm{e}} = \dot{\varepsilon}_0 \left(\frac{\sigma_{\mathrm{e}}}{g(\varepsilon^{\mathrm{P}}_{\mathrm{e}})} \right)^{1/m} \tag{2}$$

where the stress deviator is $s^{ij} = \sigma^{ij} - g^{ij}\sigma^k_k/3$, the effective von Mises stress is $\sigma_{\mathrm{e}} = \sqrt{3 s^{ij} s_{ij}/2}$, g_{ij} is the metric tensor, and $\dot{\varepsilon}_0$ is the positive reference strain rate. For a rate-hardening exponent $m \to 0$, the viscoplastic model coincides with the time-independent J_2-flow theory (Rice, 1970). The rate-hardening exponent m is usually small at room temperature ($m \approx 0.005$–0.03 for most metals, Hutchinson and Neale, 1977).

The function $g(\varepsilon^{\mathrm{P}}_{\mathrm{e}})$ represents the flow stress in a uniaxial tensile test performed at a strain rate corresponding to $\dot{\varepsilon}^{\mathrm{P}}_{\mathrm{e}} = \dot{\varepsilon}_0$ and is modelled as

$$\varepsilon^{\mathrm{P}}_{\mathrm{e}} = \frac{\sigma_0}{E} \left\{ \frac{1}{n} \left(\frac{g(\varepsilon^{\mathrm{P}}_{\mathrm{e}})}{\sigma_0} \right)^n - \frac{1}{n} + 1 \right\} - \frac{g(\varepsilon^{\mathrm{P}}_{\mathrm{e}})}{E}, \quad g(0) = \sigma_0 \tag{3}$$

where σ_0 is the reference stress, n the strain hardening exponent, and E Young's modulus.

The constitutive law for the relevant in-plane stresses (approximating a plane stress state in the shell) is given by

$$\dot{\sigma}^{\alpha\beta} = \hat{\mathscr{L}}^{\alpha\beta\gamma\delta} \dot{\eta}_{\gamma\delta} + \dot{\hat{\sigma}}^{\alpha\beta}_{*} \tag{4}$$

with

$$\hat{\mathscr{L}}^{\alpha\beta\gamma\delta} = \mathscr{L}^{\alpha\beta\gamma\delta} - \frac{\mathscr{L}^{\alpha\beta 33} \mathscr{L}^{33\gamma\delta}}{\mathscr{L}^{3333}}, \quad \dot{\hat{\sigma}}^{\alpha\beta}_{*} = \dot{\sigma}^{\alpha\beta}_{*} - \dot{\sigma}^{33}_{*} \frac{\mathscr{L}^{\alpha\beta 33}}{\mathscr{L}^{3333}}, \quad \dot{\sigma}^{ij}_{*} = -\mathscr{L}^{ijkl} \dot{\eta}^{\mathrm{P}}_{kl} \tag{5}$$

where the elastic moduli $\mathscr{L}^{ijkl}$ are given by

$$\mathscr{L}^{ijkl} = \frac{E}{1+\nu} \left\{ \frac{1}{2} (g^{ik} g^{jl} + g^{il} g^{jk}) + \frac{\nu}{1-2\nu} g^{ij} g^{kl} \right\} \tag{6}$$

and ν is Poisson's ratio.

To allow for a larger step size in the numerical analysis, a forward gradient method suggested by Peirce et al. (1984) is used. The forward gradient method is based on a linear interpolation between $\dot{\varepsilon}^{\mathrm{P}(t)}_{\mathrm{e}}$ and $\dot{\varepsilon}^{\mathrm{P}(t+\Delta t)}_{\mathrm{e}}$ of the inelastic strain rate within the increment, $\dot{\varepsilon}^{\mathrm{P}}_{\mathrm{e}} = (1-\theta)\dot{\varepsilon}^{\mathrm{P}(t)}_{\mathrm{e}} + \theta \dot{\varepsilon}^{\mathrm{P}(t+\Delta t)}_{\mathrm{e}}$, where $\dot{\varepsilon}^{\mathrm{P}(t+\Delta t)}_{\mathrm{e}}$ is found by a Tayler series expansion. An interpolation using $\theta = 0.9$ results in the largest stable step size.

3. Finite rotation shell theory

The shell theory considered does not require any assumptions concerning the magnitude of the displacement and rotation of the shell. This theory is similar to the elastic shell theory of Başar (1987), from which the notation is adopted, but in this paper the theory has been formulated for elastic–viscoplastic shells. Points on the middle surface F are described by the position vector $\mathbf{r}(\Theta^{\alpha})$, where the convected curvilinear coordinates Θ^{α} measure the position on the middle surface. Similarly, Θ^3 measures the distance from the middle surface in the direction of the base vector $\mathbf{a}_3$. Bold-face characters denote vectors. The middle surface of the shell is given by the metric tensor

$a_{\alpha\beta} = \mathbf{a}_\alpha \cdot \mathbf{a}_\beta$ and the curvature tensor $b_{\alpha\beta} = -\mathbf{a}_\alpha \cdot \mathbf{a}_{3,\beta}$, where $\mathbf{a}_\alpha = \mathbf{r}_{,\alpha}$ denotes the base vectors. Elements associated with the undeformed state are denoted ($^\circ$) while suffix-free symbols refer to the deformed state. The undeformed state is chosen as the reference state.

The Kirchhoff–Love assumption is adopted in the Lagrangian strain tensor (see Başar and Krätzig 1989, 1990)

$$\eta_{\alpha\beta} = \alpha_{\alpha\beta} + \Theta^3 \omega_{\alpha\beta} \tag{7}$$

where the membrane strain tensor $\alpha_{\alpha\beta}$ and the bending strain tensor $\omega_{\alpha\beta}$ are given, respectively, by

$$\alpha_{\alpha\beta} = \tfrac{1}{2}(\phi_{\beta\alpha} + \phi_{\alpha\beta} + \phi_{\alpha\lambda}\phi^{\lambda}_{\beta} + \phi_{\alpha 3}\phi_{\beta 3}) \tag{8}$$

and

$$\omega_{\alpha\beta} = -[\phi_{\alpha 3|\beta} + \mathring{b}^{\varrho}_{\beta}\phi_{\alpha\varrho} + w_3(\mathring{b}_{\alpha\beta} + \phi_{\alpha 3|\beta} + \mathring{b}^{\varrho}_{\beta}\phi_{\alpha\varrho}) + w_\varrho(\phi^{\varrho}_{\alpha|\beta} - \mathring{b}^{\varrho}_{\beta}\phi_{\alpha 3})] \tag{9}$$

with the deformation gradients defined by

$$\phi_{\alpha\beta} = v_{\beta|\alpha} - \mathring{b}_{\alpha\beta}v_3, \quad \phi_{\alpha 3} = v_{3|\alpha} + \mathring{b}^{\beta}_{\alpha}v_\beta \tag{10}$$

and the displacement vector given by

$$\mathbf{v} = \mathbf{r} - \mathring{\mathbf{r}} = v_\alpha \mathring{\mathbf{a}} + v_3 \mathring{\mathbf{a}}^3 \tag{11}$$

In view of the Kirchhoff–Love assumption, the three components of the difference vector can be written as (Başar and Krätzig, 1989)

$$w_\alpha = -\sqrt{\frac{\mathring{a}}{a}}(\phi_{\alpha 3} + \phi_{\alpha 3}\phi^{\beta}_{\beta} - \phi_{\beta 3}\phi^{\beta}_{\alpha})$$

$$w_3 = \sqrt{\frac{\mathring{a}}{a}}\left(1 + \phi^{\alpha}_{\alpha} + \frac{1}{2}\delta^{\alpha\beta}_{\varrho\lambda}\phi^{\varrho}_{\alpha}\phi^{\lambda}_{\beta}\right) - 1 \tag{12}$$

where $\mathring{a} = \mathring{a}_{11}\mathring{a}_{22} - \mathring{a}_{12}\mathring{a}_{21}$ and $a = a_{11}a_{22} - a_{12}a_{21}$ are the metric of the undeformed and the deformed middle surface, respectively. The generalised Kronecker's delta is given by $\delta^{\alpha\beta}_{\varrho\lambda} = \delta^{\alpha}_{\varrho}\delta^{\beta}_{\lambda} - \delta^{\alpha}_{\lambda}\delta^{\beta}_{\varrho}$, where $\delta^{\alpha}_{\lambda}$ is Kronecker's delta.

The numerical results are found by a linear incremental method, in which the non-linear shell equations are written in an incremental form (Başar and Ding, 1990).

$$\int\!\!\int_{\mathring{F}} (\overset{+}{N}{}^{\alpha\beta}\delta\overset{+}{\alpha}_{\alpha\beta} + \overset{+}{M}{}^{\alpha\beta}\delta\overset{+}{\omega}_{\alpha\beta})\,\mathrm{d}\mathring{F} + \frac{1}{2}\int\!\!\int_{\mathring{F}} (N^{\alpha\beta}\delta\overset{++}{\alpha}_{\alpha\beta} + M^{\alpha\beta}\delta\omega\alpha_{\alpha\beta})\,\mathrm{d}\mathring{F} - \int\!\!\int_{\mathring{F}} (\overset{+}{P}{}^{\alpha}\delta\overset{+}{v}_{\alpha} + \overset{+}{P}{}^{3}\delta\overset{+}{v}_3)\,\mathrm{d}\mathring{F} = \delta(\Delta W_y)$$
$$+ \left[\delta W_y - \int\!\!\int_{\mathring{F}} (N^{\alpha\beta}\delta\overset{+}{\alpha}_{\alpha\beta} + M^{\alpha\beta}\delta\overset{+}{\omega}_{\alpha\beta})\,\mathrm{d}\mathring{F} + \int\!\!\int_{\mathring{F}} (P^{\alpha}\delta\overset{+}{v}_{\alpha} + P^{3}\delta\overset{+}{v}_3)\,\mathrm{d}\mathring{F}\right] \tag{13}$$

where the bracketed term is introduced to avoid drifting of the numerical solution away from the equilibrium path. The increments are denoted $(^+) = (\dot{\ })\Delta t$, where Δt is the time step. The external

virtual work is denoted δW_y, while the membrane strain tensor $N^{\alpha\beta}$ and the moment tensor $M^{\alpha\beta}$ are defined by

$$N^{\alpha\beta} = \int_{-(h/2)}^{h/2} \sigma^{\alpha\beta}\, \mathrm{d}\Theta^3, \quad M^{\alpha\beta} = \int_{-(h/2)}^{h/2} \sigma^{\alpha\beta}\Theta^3\, \mathrm{d}\Theta^3 \tag{14}$$

where h is the thickness of the shell. The contact forces (P^α, P^3) are specified later in Section 4. The incremental variables, including an explanation of the notation $(^{++})$, are given in Appendix A. In eqn (14) it is assumed that the radius R of the shell is large compared with h such that $|1+\Theta^3 R| \approx 1$ (see Başar and Krätzig, 1990).

If the rotation of the shell is small such that $\mathbf{w} = \mathbf{a}_3 - \mathring{\mathbf{a}}_3 \approx \mathbf{0}$, the bending strain tensor reduces to $\omega_{\alpha\beta} = -\phi_{\alpha 3|\beta} - \mathring{b}^{\varrho}_{\beta}\phi_{\alpha\varrho}$ and the shell theory will therefore coincide with the moderate rotation shell theory (Niordson, 1985) used in e.g. Mikkelsen (1995).

4. Contact formulation

A number of different numerical procedures for treating contact problems have been developed in the literature. In the case of collapsing shell structures, the main complexity is that some unknown part of the shell will come into contact with some other part (see e.g. Benson and Hallquist, 1990). Therefore, the traditional approach of defining master and slave contact surfaces is not possible. On the other hand, an accurate contact formulation is not essential for the collapse behaviour. The major component of energy is absorbed during collapse by deformation of the shell walls. The purpose of the contact formulation presented here is therefore only to prevent the shell from penetrating itself while ensuring a stable numerical solution. In the contact formulation, a contact middle surface is used which differs slightly from the smooth curved middle surface of the finite element model (see Fig. 1(a)). The contact surface is defined by flat elements connecting the finite element nodes.

Contact is obtained when the penetrating node S and the contact element AB (see Fig. 1(b)) satisfy the conditions

$$d < h, \quad L_A > 0, \quad L_B > 0 \tag{15}$$

where

$$d = |\mathbf{r}_{AS} \cdot \mathbf{n}|, \quad L_A = \mathbf{r}_{AS} \cdot \mathbf{r}_{AB}/L_{AB} \quad \text{and} \quad L_B = -\mathbf{r}_{BS} \cdot \mathbf{r}_{AB}/L_{AB} \tag{16}$$

and the unit vector $\mathbf{n}$ is the normal to the contact element AB. At contact, the contact force on the penetrating node S is evaluated as

$$\mathbf{F} = KL_S(h-d)\alpha\mathbf{n}, \quad \alpha = \begin{cases} 1 & \text{for } \mathbf{r}_{AS} \cdot \mathbf{n} > 0 \\ -1 & \text{for } \mathbf{r}_{AS} \cdot \mathbf{n} < 0 \end{cases} \tag{17}$$

where L_S is the average element length of the two elements containing node S. The stiffness K of the contact spring is chosen as high as possible without destabilising the numerical solution. The reaction forces on the contact element ($\mathbf{F}_A, \mathbf{F}_B$) are simply applied according to the lengths L_A and L_B in Fig. 1(b), such that

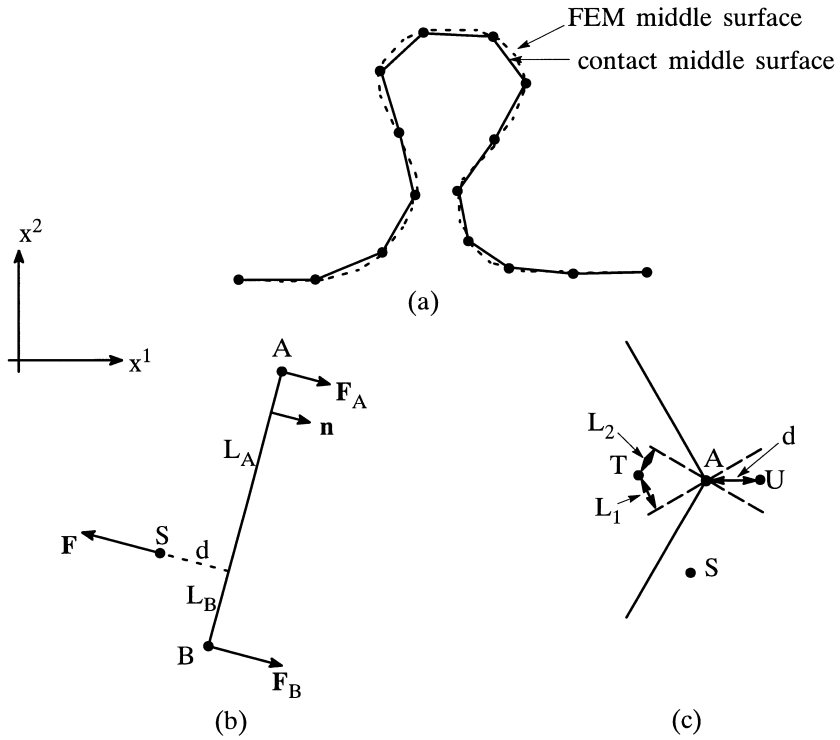

Fig. 1. (a) Contact middle surface and middle surface for the finite element method model. (b) Contact forces between a penetrating finite element node S and the contact element AB. (c) The three possibilities of contact of the penetrating node (S, T and U) and the contact surface.

$$\mathbf{F}_A = -\mathbf{F}L_B/L_{AB}, \quad \mathbf{F}_B = -\mathbf{F}L_A/L_{AB} \tag{18}$$

The increment of the contact forces ($\overset{+}{\mathbf{F}}$, $\overset{+}{\mathbf{F}}_A$ and $\overset{+}{\mathbf{F}}_B$) can now be evaluated from

$$\overset{+}{\mathbf{F}} = -K\overset{+}{d}\alpha\mathbf{n}, \quad \overset{+}{d} = \alpha(\overset{+}{\mathbf{r}}_{AS}\cdot\mathbf{n}+\mathbf{r}_{AS}\cdot\overset{+}{\mathbf{n}}) \tag{19}$$

where the increment of the vectors $\overset{+}{\mathbf{r}}_{AS}$ and $\overset{+}{\mathbf{n}}$ is evaluated from its components, which are given by the increments of the displacements $\overset{+}{v}_1$ and $\overset{+}{v}_3$ at the nodes A, B and S

$$\overset{+}{\mathbf{r}}_{AS} = \begin{pmatrix}\overset{+}{v}_1\\ \overset{+}{v}_3\end{pmatrix}_S - \begin{pmatrix}\overset{+}{v}_1\\ \overset{+}{v}_3\end{pmatrix}_A \quad \text{and} \quad \overset{+}{\mathbf{n}} = \frac{1}{L_{AB}}\left[\begin{pmatrix}-\overset{+}{v}_3\\ \overset{+}{v}_1\end{pmatrix}_B - \begin{pmatrix}-\overset{+}{v}_3\\ \overset{+}{v}_1\end{pmatrix}_A\right] \tag{20}$$

The disadvantages of using straight contact elements appear when the node S penetrates the contact surface near a node (see Fig. 1(c)). Two cases must be treated separately. When node T penetrates two contact elements simultaneously or when node U moves between two contact elements. In the first case, the contact forces are weighted with the factors $L_1/(L_1+L_2)$ and $L_2/(L_1+L_2)$, respectively, according to the lengths L_1 and L_2 in Fig. 1(c). In the second case, the contact forces are found according to the distance d between the nodes A and U (see Fig. 1(c)). The contact forces are then given by

$$\mathbf{F} = KL_S(h-d)\mathbf{m} \quad \text{with } \mathbf{m} = \mathbf{r}_{AU}/|\mathbf{r}_{AU}| \tag{21}$$

where the reaction force on A is $\mathbf{F}_A = -\mathbf{F}$. The corresponding increments are given by

$$\overset{+}{\mathbf{F}} = -KL_S\overset{+}{d}\mathbf{n} \quad \text{with } \overset{+}{d} = \mathbf{r}_{AU}\overset{+}{\mathbf{r}}_{AU}/|\mathbf{r}_{AU}| \tag{22}$$

As no part of the shell can be treated as master or slave contact surface prior to the numerical analysis, all the finite element nodes are treated as possible penetrating nodes. Therefore, in most cases, there will be contact both ways between the shell walls, resulting in twice the number of contact forces.

The contact forces between the shell walls are introduced into the principle of virtual work in incremental form (13) by adopting

$$\begin{aligned}
\int_{\mathring{F}}\int(\overset{+}{P}^{\alpha}\delta\overset{+}{v}_{\alpha} + \overset{+}{P}^{3}\delta\overset{+}{v}_{3})\,\mathrm{d}\mathring{F} &= \sum_{k=1}^{\text{nodes}}(\overset{+}{F}^{\alpha}\delta\overset{+}{v}_{\alpha} + \overset{+}{F}^{3}\delta\overset{+}{v}_{3}) \\
\int_{\mathring{F}}\int(P^{\alpha}\delta\overset{+}{v}_{\alpha} + P^{3}\delta\overset{+}{v}_{3})\,\mathrm{d}\mathring{F} &= \sum_{k=1}^{\text{nodes}}(F^{\alpha}\delta\overset{+}{v}_{\alpha} + F^{3}\delta\overset{+}{v}_{3})
\end{aligned} \tag{23}$$

Contact between the shell walls and an outer boundary (symmetry and clamped boundary condition) depends on the penetration of the Gauss integration points into the outer boundary. Therefore, the integrals in (23) for the contact forces (P^1, P^3) and their increments ($\overset{+}{P}^1$, $\overset{+}{P}^3$) can be evaluated directly. The contact forces are, as above, modelled to be proportional to the penetration depth.

5. Numerical approach and results

Numerical results were obtained by a finite element analysis for an axially compressed cylindrical shell. The geometry of the shell analysed is specified by the length L, the radius R and the wall thickness h. In experimental work, Johnson et al. (1977) found that tubes made of PVC material were $4 < R/h < 13$ collapse first in one concertina fold followed by a diamond pattern fold. Stainless steel and aluminium specimens having $8 < R/h < 16$ collapse in concertina failure, while tubes with $R/h \approx 16$ collapse in a diamond failure. Allan (1968) observes that tubes with a wall thickness down to $R/h \approx 70$ will collapse in a concertina pattern, whereas the thinner tubes tend to form a diamond pattern after one or more folds.

The present numerical finite element analysis assumes that a concertina collapse mode will dominate (see Fig. 2). Here, tubes in the region $35 < R/h < 100$ are analysed. These values of R/h have been chosen as a compromise between the requirement of a concertina collapse mode and satisfying the small strain theory and a large r/h ratio of the deformed shell (see later in the discussion). Even though the thinnest tube would in practice only collapse in a concertina mode for a very extreme material parameter, the results for the thinner tubes are included here only as a parameter study.

The shell is discretised in the axial direction, where the displacement increments in an element are approximated by Hermitian cubics in each element. The integration in the axial direction is

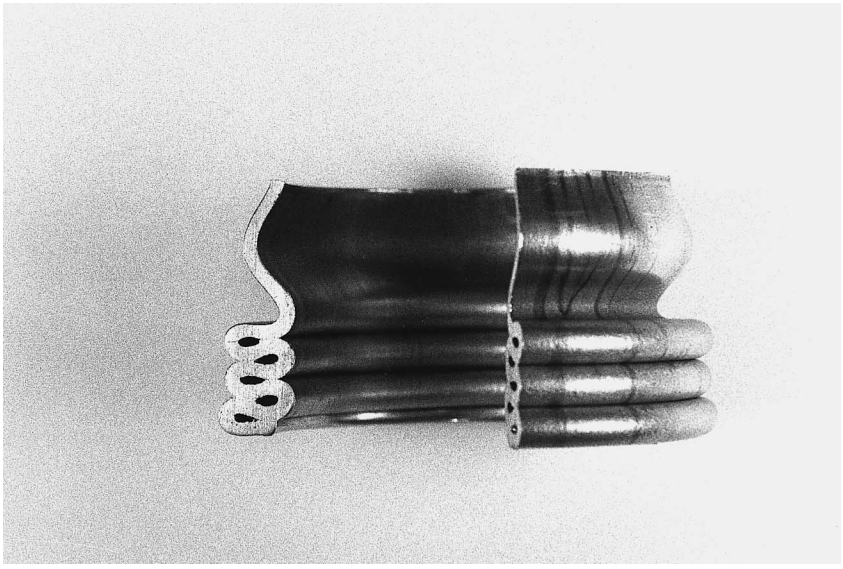

Fig. 2. Saw-cut through an axisymmetric collapsed thickwalled aluminium shell with $R/h = 14$.

performed by a three-point Gauss integration scheme, while the integration at each Gauss integration point in the thickness direction (Θ^3) is performed by a seven-point Simpson integration. The axisymmetric analysis is performed by fixing the displacement $v_2 = 0$ and the gradients $\partial v_i/\partial\Theta^2 = 0$. A linear Euler integration over the time increment Δt is used to update the stress tensor $\sigma^{\alpha\beta}$, the inelastic strain ε_e^P in the Gauss and Simpson integration points and the displacements of the nodes. The numerical scheme used is similar to that used by Tvergaard (1983a) and Mikkelsen (1993).

The buckling behaviour can be initiated by deformations resulting from the boundary conditions or by an initial localised imperfection (Tvergaard, 1983a; Mikkelsen, 1995). In the present paper, both a geometrically perfect shell with a clamped edge and a shell with an initially localised imperfection are analysed. In the latter case, the localised imperfection is given as

$$\bar{v}_3 = \bar{\xi} h\, e^{-4\beta(\Theta^1/L-1)^2} \sin\frac{\pi\Theta^1}{l_c} \tag{24}$$

The parameter β specifies the degree of localisation and $\bar{\xi}$ the amplitude of the imperfection. The length l_c denotes the critical half-wave length for the corresponding time-independent case ($m \to 0$) (Tvergaard, 1983; Mikkelsen, 1995). For the shell with an initial localised imperfection, the boundary conditions at both ends of the shell are assumed to be symmetric, while the clamped shell is clamped at the edge $\Theta^1 = L$. In all the numerical examples, the parameter β is chosen to be $\beta = 55$, which corresponds to an initially strongly localised imperfection with an imperfection amplitude below $\bar{\xi}/100$ when $|L-\Theta^1| < 0.14L$.

For a sufficiently small initial imperfection and a sufficiently thick-walled shell, the collapse behaviour will normally be initiated by boundary effects. In Fig. 3, a clamped initially geometrically perfect shell, with a radius/thickness ratio $R/h = 100$, is analysed. The elastic–viscoplastic material

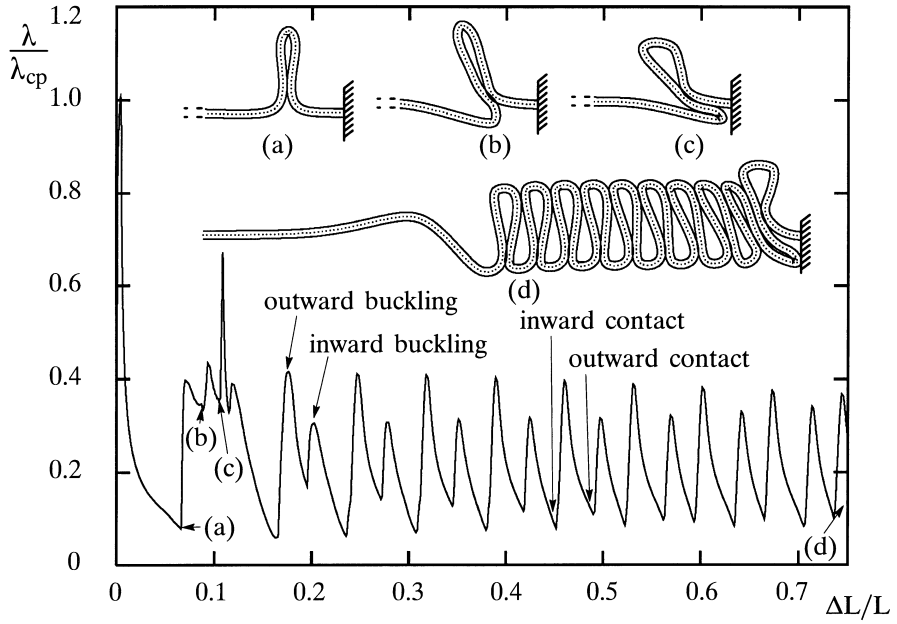

Fig. 3. Axial load vs shortening for a geometrically perfect clamped viscoplastic cylindrical shell with $R/h = 100$, $\sigma_0/E = 0.001$, $n = 10$, $\nu = 0.3$, $m = 0.05$, $L = 15l_c$ and $\dot{\varepsilon}_L = \dot{\varepsilon}_0$. (a–c) Formation of the first collapse fold. (d) Collapse mechanism when the compressed length is equal to 25% of the initial length.

is specified by a reference stress $\sigma_0/E = 0.001$, a strain hardening exponent $n = 10$, Poisson's ratio $\nu = 0.3$, and the rate-hardening exponent $m = 0.05$. The length of the shell is $L = 15l_c$, where the critical half-wave length for the corresponding time-independent case is $l_c = 0.19R$, with the corresponding critical stress $\sigma_{cp} = 1.38\sigma_0$ (axisymmetric plastic bifurcation load). The load $\lambda_{cp} = 2\pi hR\sigma_{cp}$ is used to normalise the axial load in the load vs. shortening curve. In Fig. 3, the average shortening strain rate $\dot{\varepsilon}_L = \dot{\Delta}L/L$ is prescribed to be equal to the reference strain rate $\dot{\varepsilon}_L = \dot{\varepsilon}_0$. Figure 3(a–d) show the deformed wall of the upper part of the cylindrical shell at four different stages of deformation. The dots denote the finite element nodes on the middle surface, while the shell surfaces (solid curves) are evaluated from the deformed middle surface base vector $\mathbf{a}_3$.

The local maxima and minima on the load vs shortening curve occur as a result of the progressive development of new outward and inward buckles. The load minima is reached when the collapse fold is fully developed just before new contact develops between the shell walls. The load peak for the initial buckling behaviour ($\lambda_{max} = 1.01\lambda_{cp}$) is reached at a very early stage of deformation. At this stage, some axisymmetric buckles with small amplitude have just started to develop near the clamped boundary, see e.g. Mikkelsen (1995). The half-wave length l_i of these buckles differs only slightly from the half-wave length for the corresponding time-independent case ($l_i = 0.96l_c$). After reaching the load peak for the first buckle, the load carrying capacity of the shell drops drastically to only 10% of λ_{cp}. At this point, the first outward fold is fully developed and contact between the shell walls has occurred (see Fig. 3(a), which corresponds to point a on the load vs. shortening

curve). The following inward collapse fold develops through combined sliding and deformation of the shell walls between point b (Fig. 3(b)) and point c (Fig. 3(c)). The load peak just after point c occurs when contact between the shell walls and the clamped edge occurs.

After the first collapse fold has formed ($\Delta L/L > 0.16$), the progressive inward and outward folding process is nearly periodic. The final folding pattern (Fig. 3(d)) is seen to have a tendency to "capsize" towards the clamped edge for the fold away from the edge. This may be due to the fact that the width (i.e. axial length of the fully developed inward fold) is slightly larger than the width of the outward fold. A tendency which is also seen in saw-cuts of crushed tubes (see e.g. Grzebieta, 1990; Wierzbicki et al., 1992; Singace et al., 1995; Singace and Elsobky, 1996 and also Fig. 2). This "capsize" tendency results in a decreasing outward contact load and a slightly increasing inward contact load during the progressive folding. In spite of the fact that the half-wave length l_i of the initial buckling pattern is the critical half-wave length for the corresponding time-independent case ($l_i = 0.96l_c$), the final lengths of the folds differ significantly. Excluding the first developed fold near the clamped boundary, the average length of the undeformed middle surface for one half fold is $l_f = 0.64l_c$. The eccentricity factor introduced by Wierzbicki et al. (1992) is defined as the ratio between the length of the middle surface of the outward fold (compared with the unfolded tube) and the total folding length (l_f). In Fig. 3d, the eccentricity factor is found to lie between 0.59–0.63 in the near periodic region. Experimental measurement, carried out by Singace and Elsobky (1996), produced an eccentricity factor between 0.60 and 0.63. For completeness, it should be mentioned that, in the following numerical results, a larger range of the eccentricity factor has been found, i.e. a range between 0.55–0.70 in the near periodic region for the examples shown in Figs 3–6.

In Fig. 4, the shell is assumed to collapse far from the edges. Therefore, the clamped boundary condition at $\Theta^1 = L$ (the right end of the tube in Fig. 3a–d) is replaced by a symmetric boundary condition and the initial buckling behaviour is now initiated by an initial localised imperfection (24) with an imperfection amplitude given by $\bar{\xi} = 0.01$ and $\beta = 55$. This corresponds to a shell of length $2L$ which collapses in the middle ($\Theta^1 = L$). The material parameter and geometry of the shell are chosen to be the same as in Fig. 3. While the development of the first fold (Fig. 4(a)) is initiated by the initial imperfection, the following fold (Fig. 4(b), (c)) will mainly be initiated by a bulge developed due to the previously developed fold. The average fold length in the near periodic region, $l_f = 0.63l_c$, is seen to be close to the half-fold length found in Fig. 3. A way to measure the ability of a shell structure to absorb energy during collapse is characterised by the mean carrying capacity (λ_m) of the shells. In the near periodic region, the mean load during a whole number of folds is seen to differ only slightly between Fig. 3 and Fig. 4 (2–3%), while the difference is slightly larger (5–6%) for the total structural collapse ($0 < \Delta L < 0.75L$). Therefore, only the development of the first one of two folds is dependent on the actual boundary condition, while the following collapse behaviour is rather independent. Therefore, the collapse modes in the near periodic region shown in Fig. 3(d) and Fig. 4(d) are comparable with the collapse mode found experimentally in Fig. 2, even though the boundary conditions are not similar. On the other hand, an experimental verification of the initial collapse behaviour would also require a detailed knowledge of the shape and amplitude of initial imperfections.

Figure 5 shows the collapse behaviour for the corresponding time-independent case (J_2-flow theory). Compared with the viscoplastic shell in Fig. 4, the mean load λ_m in Fig. 5 (both in the near periodic region and during the full structural collapse) is found to be 9% lower. For the time-

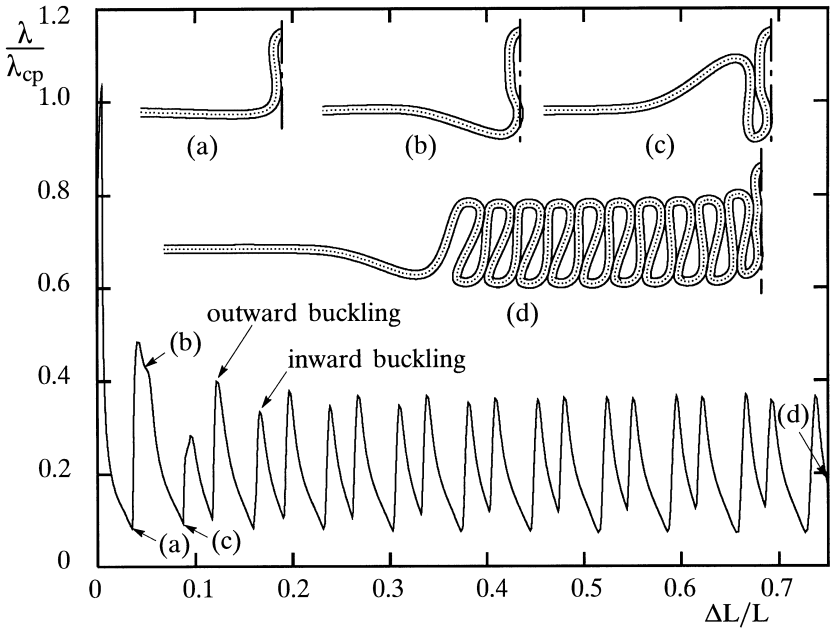

Fig. 4. Axial load vs shortening for an initially imperfect ($\beta = 55$ and $\bar{\xi} = 0.01$) viscoplastic shell with $R/h = 100$, $\sigma_0/E = 0.001$, $n = 10$, $\nu = 0.3$, $m = 0.05$, $L = 15l_c$ and $\dot{\varepsilon}_L = \dot{\varepsilon}_0$. (a–c) Formation of the first collapse fold. (d) Collapse mechanism at a compressed length equal to 25% of the initial length.

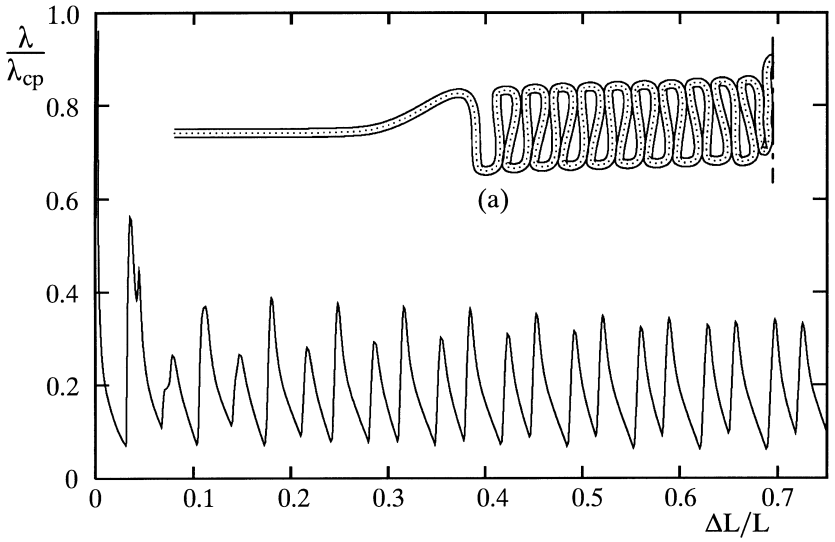

Fig. 5. Axial load vs shortening for an initially imperfect ($\beta = 55$ and $\bar{\xi} = 0.01$) time-independent shell with $R/h = 100$, $\sigma_0/E = 0.001$, $n = 10$, $\nu = 0.3$, $L = 15l_c$. (a) The collapse mechanism at a compressed length equal to 25% of the initial length.

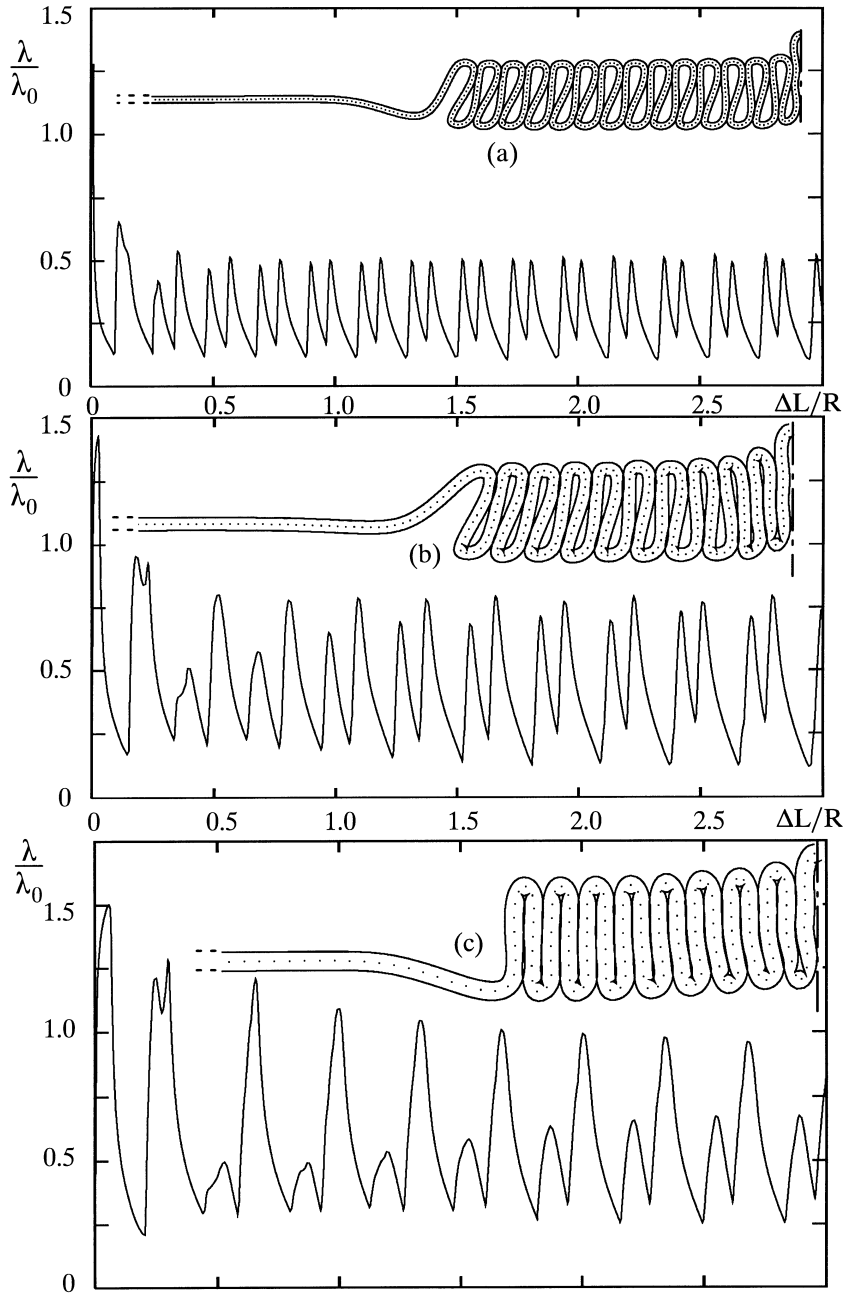

Fig. 6. Axial load vs shortening curves for three initially imperfect ($\beta = 55$ and $\bar{\xi} = 0.1$) viscoplastic shells with a viscoplastic material given by $\sigma_0/E = 0.001$, $n = 10$, $\nu = 0.3$, $m = 0.05$ compressed at a rate given by $\dot{\varepsilon}_L = \dot{\varepsilon}_0$. The radius thickness ratio is given by (a) $R/h = 100$ ($L = 21l_c$), (b) $R/h = 50$ ($L = 15l_c$) and (c) $R/h = 35$ ($L = 15l_c$). The deformation state is shown at a compression equal to $\Delta L = 3R$.

independent case (compared with the viscoplastic shell, Fig. 4) the axial length of the collapse fold is found to be significantly shorter. The axial length of one compressed fold is found to be $L_d = 3.4h$ in Fig. 5, compared with $L_d = 3.8h$ in Fig. 4 ($L_d = 2.0h$ corresponds to a totally flattened fold). The difference in L_d for the time-dependent and time-independent case is due to the fact that even though the overall prescribed shortening rate in Fig. 4 is $\dot{\varepsilon}_L = \dot{\varepsilon}_0$, the shell material will actually be deformed at a much higher rate than $\dot{\varepsilon}_L$. Only a small zone around the actually developing collapse fold is deformed at a given point in the deformation history. Therefore, due to the rate-hardening effects, the collapse of the viscoplastic shell in Fig. 4, compared with Fig. 5, appears at a higher stress level and with a consequently greater radius of curvature of the developed collapse folds.

Figure 6(a–c) show the sensitivity of the viscoplastic collapse behaviour to the radius to thickness ratio. Due to the different radius to thickness ratios, the three shells following the corresponding time-independent J_2-flow theory have different critical stresses σ_{cp} and critical half-wave lengths l_c. Therefore, to make the three curves directly comparable, the shortening is normalised with the radius R (instead of L) and the axial load with $\lambda_0 = 2\pi hR\sigma_0$ (instead of $\lambda_{cp} = 2\pi hR\sigma_{cp}$). The critical time-independent bifurcation stresses are given by $\sigma_{cp} = 1.38\sigma_0$, $\sigma_{cp} = 1.57\sigma_0$ and $\sigma_{cp} = 1.67\sigma_0$ for the three shells with $R/h = 100$, $R/h = 50$ and $R/h = 35$, respectively. At a compression $\Delta L = 3R$, the lowest number of folds is seen for the thickest shell. Correspondingly, the folding length is also seen to increase from $l_f = 0.12R$ for the shell with $R/h = 100$ to $l_f = 0.20R$ for the shell with $R/h = 35$. The minimum radius of curvature of the deformed middle surface r relative to the shell thickness is also seen to be sensitive to the radius to thickness ratio. The smallest radius of curvature is obtained for the thickest shell. This effect can be seen as a decrease in the axial length of a deformed fold. The axial length of a fold is found to be $L_d = 3.9h$, $L_d = 2.7h$ and $L_d = 2.0h$ for (a) $R/h = 100$, (b) $R/h = 50$ and (c) $R/h = 35$, respectively. Figure 6(c) with $L_d = 2.0h$ is seen to correspond to a total flattening of the compressed collapse fold with contact along the whole fold. The ability of the shells to absorb energy is found to be highly dependent on the radius to thickness ratio. A comparison of the shell for $R/h = 100$ with the shell for $R/h = 35$ shows that the mean load λ_m in the near periodic region, and therefore also the energy absorption, increases by 103% from $\lambda_m = 0.29\lambda_0$ for $R/h = 100$ to $\lambda_m = 0.59\lambda_0$ for $R/h = 35$. For comparison, the critical stress for the corresponding time-independent case increases by only 21%.

Figure 7 illustrates the sensitivity of the viscoplastic collapse behaviour to the prescribed shortening rate. The rate-hardening exponent of the shell material is $m = 0.05$. The shell is compressed at two different shortening rates corresponding to an average axial strain rate equal to $\dot{\varepsilon}_L^a = \dot{\varepsilon}_0/10$ or $\dot{\varepsilon}_L^b = 10\dot{\varepsilon}_0$, respectively. The increased shortening rate is found to have an insignificant effect on the collapse pattern, while the effect on the load level is significant. The maximum load carrying capacity (initial load peak) increases by 25% and the mean load during the collapse for $0 < \Delta L/L < 0.5$ is 24% higher. An explanation may be based directly on the viscoplastic constitutive law (2). If the elastic part of the strain tensor is negligible, two different deformation rates $\dot{\varepsilon}_L^a$ and $\dot{\varepsilon}_L^b$ will result in little difference between $\varepsilon_e^p|^a$ and $\varepsilon_e^p|^b$ and between $s_{ij}/\sigma_e|^a$ and $s_{ij}/\sigma_e|^b$ in any part of the structure. Essentially, the same deformation pattern will develop, the only difference being that the deformation rate is higher at a higher stress level as specified by $\sigma_e^b/\sigma_e^a = (\dot{\varepsilon}_L^b/\dot{\varepsilon}_L^a)^m$. In Fig. 7 this corresponds to $\sigma_e^b/\sigma_e^a = 1.26$. The shell in Fig. 7 is compressed well into the inelastic region ($\sigma_{cp} = 1.57\sigma_0$) before the initial buckling behaviour develops. During the development of the following collapse fold, some parts of the structure undergo unloading. Even though these parts have a dominant elastic contribution in the strain tensor, the influence on the deformation

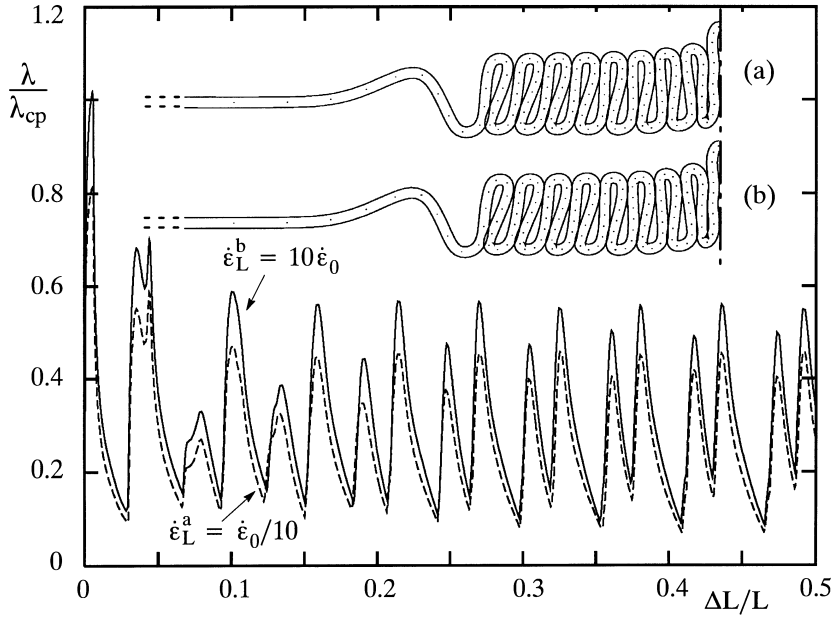

Fig. 7. Axial load vs shortening for an initially imperfect viscoplastic shell ($\beta = 55$ and $\bar{\xi} = 0.1$) with $R/h = 50$, $\sigma_0/E = 0.001, n = 10, \nu = 0.3, m = 0.05$ and $L = 15l_c$, for two different compression rates, and the corresponding collapse mode (a–b) at a compression equal to 50%.

pattern is insignificant. Therefore, the final collapse pattern is quite insensitive to the shortening rate (Fig. 7(a) and (b)), while the stress level grows proportionally to the factor $(\dot{\varepsilon}_L^b/\dot{\varepsilon}_L^a)^m$.

Using the shell as a shock absorbing device, an obvious requirement is a high energy absorption of the shell structure during total structural collapse without any dangerously high load peaks. Figure 8 demonstrates a method for controlling the height of the initial load peak by introducing a large initial localised imperfection (axisymmetric bulge) into the shell structure. Even though, this imperfection significantly lowers the energy absorption during the formulation of the first fold (see also Mikkelsen, 1995), the overall energy absorption during total structural collapse (development of a larger number of folds) is almost unchanged. Using an imperfection amplitude $\xi = 1.0$ (Fig. 8(b)) instead of $\xi = 0.1$ (Fig. 8(a)) is seen to reduce the initial load peak by 35% while the energy absorption of the shell during 50% compression decreases by only 7%. Applying an even larger imperfection $\xi = 10$ (Fig. 8c) is seen to result in a collapse behaviour in which the initial load peak is below the load oscillation during the structural collapse. The difference in the energy absorption for the three shells (Fig. 8a–c) in the near periodic regions is found to be below 2%. A larger imperfection amplitude is seen to give a somewhat smaller number of developed collapse folds at 50% compression. This is due to the fact that the imperfection is prescribed by the critical half-wave length for the corresponding time-independent case, while the average length of the folds developed in the near periodic region is smaller, $l_f = 0.50l_c$.

Inertia effects are neglected in the presented analysis in spite of their obvious influence on the load peaks of a shock absorbing device. As shown by a dynamic analysis of a simple three-hinge,

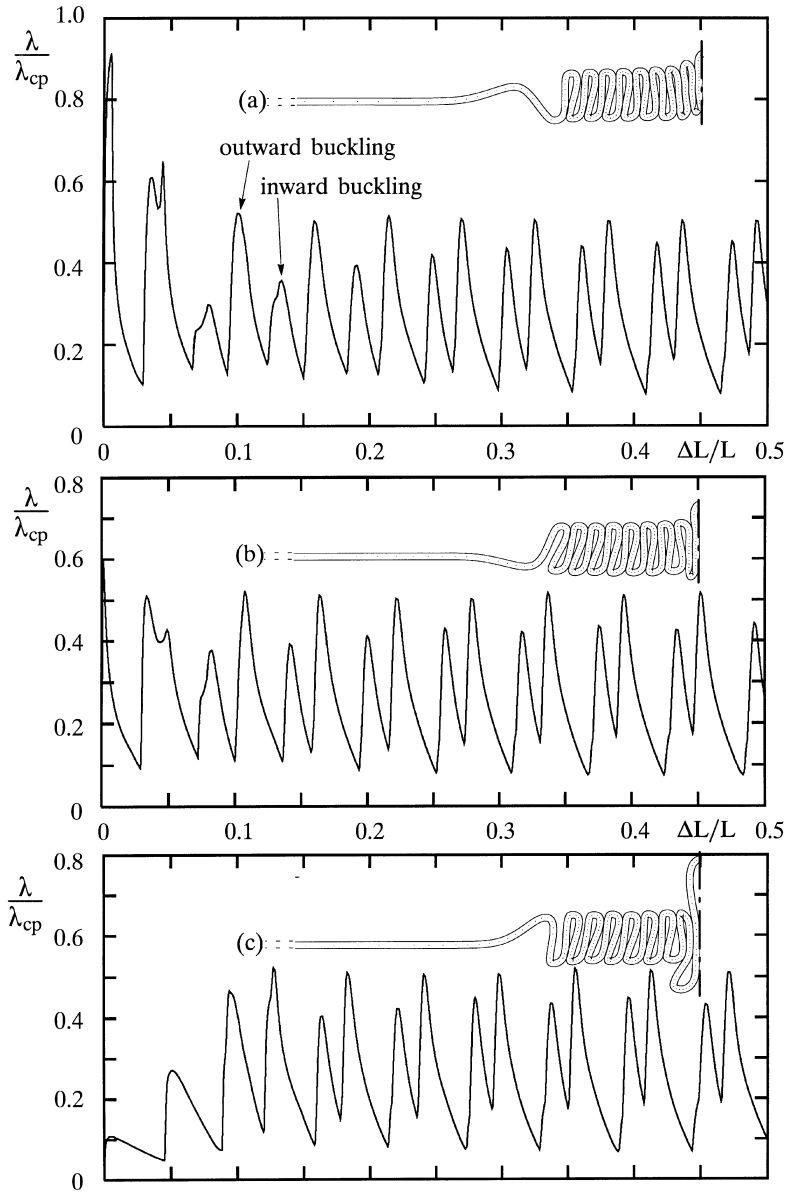

Fig. 8. Axial load vs shortening curve and the collapse mode at 50% compression for viscoplastic shells with $R/h = 50$, $\sigma_0/E = 0.001$, $n = 10$, $\nu = 0.3$, $m = 0.05$, $\dot{\varepsilon}_L = \dot{\varepsilon}_0$ and $L = 15l_c$. Three shells are analysed with a localised imperfection given by $\beta = 55$ and an imperfection amplitude of (a) $\bar{\xi} = 0.1$, (b) $\bar{\xi} = 1.0$ and (c) $\bar{\xi} = 10$, respectively.

rigid-rod model performed by Hutchinson and Budiansky (1966), the maximum load is much increased by the effect of inertia when imperfections are small. Nevertheless, as also indicated by this analysis of Hutchinson and Budiansky (1966), the importance of the inertia effects decreases

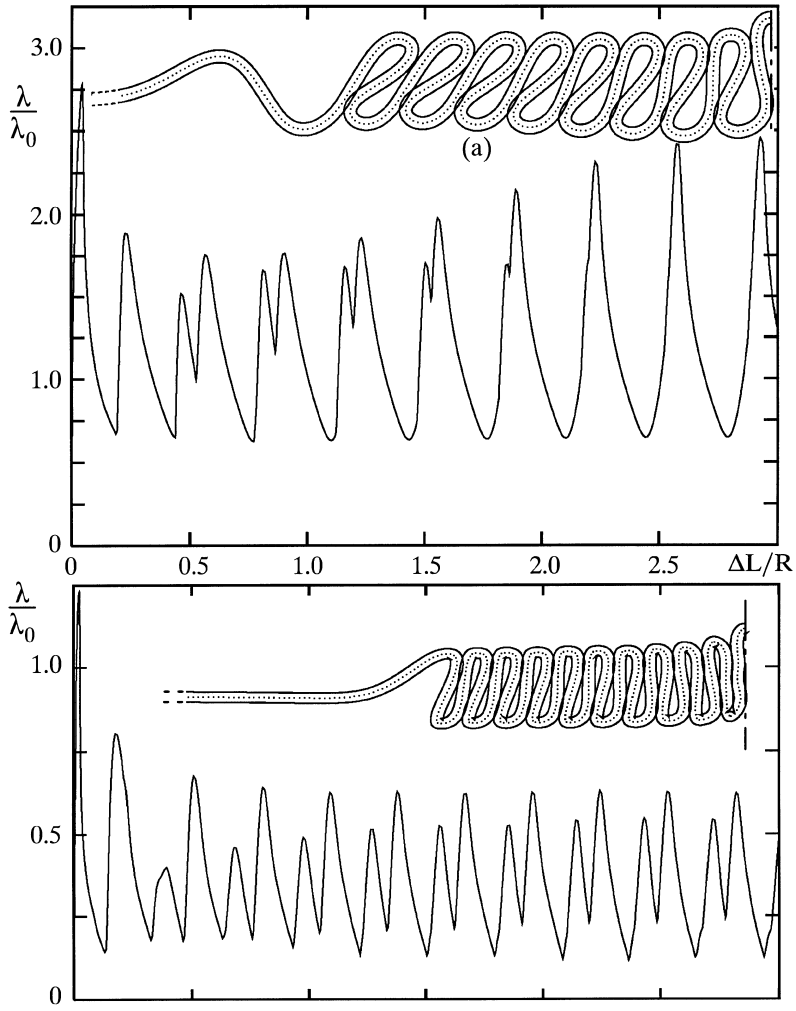

Fig. 9. Axial load vs shortening curves for initially imperfect ($\beta = 55$ and $\bar{\xi} = 0.1$) shells with $R/h = 50$, $v = 0.3$, $m = 0.05$, $L = 19l_c$ and $\dot{\varepsilon}_L = \dot{\varepsilon}_0$. Two shells with different materials are analysed (a) $\sigma_0/E = 0.001$ and $n = 3$; (b) $\sigma_0/E = 0.0025$ and $n = 10$. The deformation states are shown at a compression equal to $\Delta L = 3R$.

drastically with increasing initial imperfection. Therefore, the presence of a large initial imperfection will not only reduce the static initial buckling load, as shown above, but will also reduce the difference between the static and dynamic buckling loads.

Compared with Fig. 6(b), Fig. 9 shows the effect of using a shell material with a lower strain-hardening exponent n (Fig. 9(a)) or a higher reference stress σ_0 (Fig. 9(b)). A change in the strain-hardening exponent from $n = 10$ (Fig. 6(b)) to $n = 3$ (Fig. 9(a)) results in a 177% increase in the mean load in the near periodic region, from $\lambda_m = 0.44\lambda_0$ to $\lambda_m = 1.22\lambda_0$. The critical bifurcation stress σ_{cp} for the corresponding time-independent case is correspondingly increased by 126%. The final collapse fold is highly influenced by the strain hardening of the shell material. Even though the

critical half-wave length l_c for the corresponding time-independent case decreases from $l_c = 0.34R$ ($n = 10$) to $l_c = 0.25R$ ($n = 3$), the final half-fold length is found to increase from $l_f = 0.17R$ to $l_f = 0.21R$. The length of a compressed fold is correspondingly increased from $L_d = 2.8h$ ($n = 10$) to $L_d = 4.2h$ ($n = 3$).

A change in the reference stress of the shell material (from $\sigma_0/E = 0.001$ in Fig. 6(b) to $\sigma_0/E = 0.0025$ in Fig. 9(b)) results only in a small difference in the developed collapse fold. The critical half-wave length for the corresponding time-independent case is shortened from $l_c = 0.34R$ ($\sigma_0/E = 0.001$) to $l_c = 0.25\ R$ ($\sigma_0/E = 0.0025$), while the final collapse fold length differs by less than 1% between the two cases. The corresponding length of a compressed fold is $L_d = 2.6h$ in Fig. 9(b) and $L_d = 2.7h$ in Fig. 6(b). The mean load λ_m in the near periodic region changes significantly from $\lambda_m = 4.2 \cdot 10^{-4}\lambda_E$ ($\sigma_0/E = 0.001$) to $\lambda_m = 9.0 \cdot 10^{-4}\lambda_E$ ($\sigma_0/E = 0.0025$). Note that $\lambda_E = 2\pi hRE$ is used to normalise the mean load. This is an increase by 114%, which should be compared with the corresponding 150% increase in the reference stress σ_0 and the 112% increase in σ_{cp}.

6. Comparison with analytical approaches

For time-independent material behaviour it is possible to derive a simplified collapse approach by neglecting the elastic strain and the strain hardening ($n \to \infty$). Alexander (1960) considers a purely outward collapse mode in which one collapse fold is developed around three plastic hinges, resulting in a final developed collapse fold with an axial length of only $L_d = 2h$. The half folding length l_f and the mean carrying capacity λ_m is found by Alexander (1960) to be

$$\frac{l_f^{Al}}{R} = 1.35\sqrt{\frac{h}{R}}, \quad \frac{\lambda_m^{Al}}{\lambda_0} = 1.34\sqrt{\frac{h}{R}} + 0.29\frac{h}{R} \tag{25}$$

Abramowicz and Jones (1984) replace Alexanders folding mechanism by a mechanism in which the outward fold is divided into two equal mirrored parts with the same constant curvature r. The axial length of a developed fold will then be $L_d = h + 2r$. The half folding length and the mean load are found by Abramowicz and Jones (1984) to be

$$\frac{l_f^{AJ}}{R} = 1.24\sqrt{\frac{h}{R}}, \quad \frac{\lambda_m}{\lambda_0} = \frac{1.170\sqrt{h/R} + 0.474h/R}{0.86 - 0.40\sqrt{h/R}} \tag{26}$$

Grzebieta (1990) modified Abramowicz and Jones' outward collapse mechanisms slightly and thereby found an estimate of the load variation during one collapse fold. This collapse mechanism was used by Gupta and Velmurngan (1995) in a re-examination which considered a simultaneously developed outward and inward collapse fold. Both approaches result in only one load peak during one collapse fold, despite the fact that development of one collapse fold will result in two load peaks. Wierzbicki et al. (1992) simulate two load peaks by suggesting a collapse mechanism with a distinct progressive inward and outward collapse behaviour. Based on this assumption, Singace et al. (1995) found

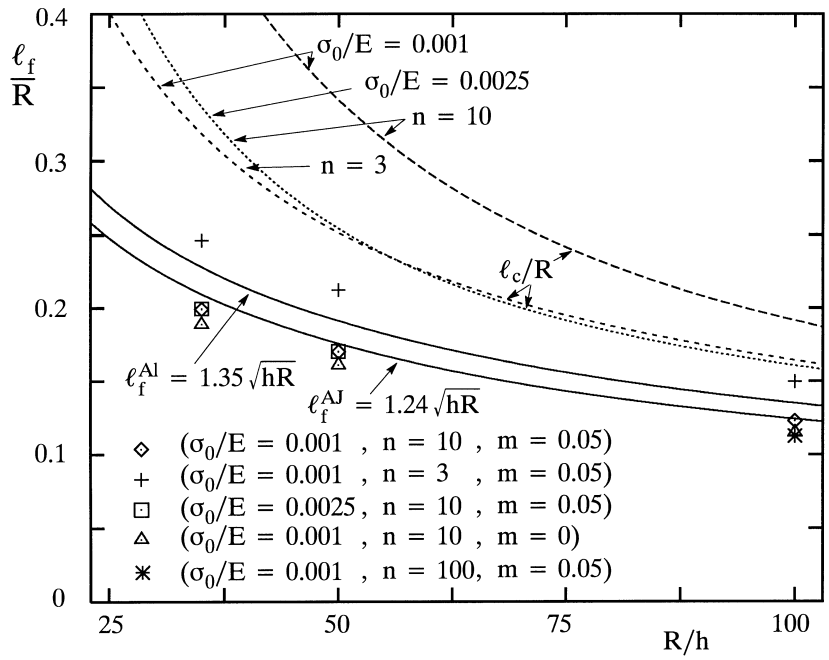

Fig. 10. The half folding length in the near periodic area for the analysed cylindrical shells with localised imperfection ($\beta = 55$ and $\bar{\xi} = 0.1$ or $\bar{\xi} = 0.01$) compared with the critical half-wave length l_c and the half folding length from two approximative models l_f^{Al} (Alexander, 1960) and l_f^{AJ} (Abramowicz and Jones, 1984).

$$\frac{l_f^{SER}}{R} = 1.25\sqrt{\frac{h}{R}}, \quad \frac{\lambda_m^{SER}}{\lambda_0} = 1.25\sqrt{\frac{h}{R}} + 0.22\frac{h}{R} \tag{27}$$

In Fig. 10, the folding length of the developed folds in the near periodic region (see Section 5) is compared with the critical half-wave length l_c for the corresponding time-independent case (dashed curves) and the half folding length found by the approaches (25) and (26). Note that the half folding length from (27) $l_f^{SER} \approx l_f^{AJ}$. The symbols ($\diamond + \boxdot \triangle *$) in Fig. 10 indicate the half folding length for the shells analysed in Figs 4–6 and 9, in addition to some similar cases (initial localised imperfection) with $L = 15l_c$, $\beta = 55$ and $\bar{\xi} = 0.1$ compressed at a rate $\dot{\varepsilon}_L = \dot{\varepsilon}_0$. Nevertheless, as l_f is evaluated from the collapse fold in the near periodic region and is therefore rather insensitive to the previously developed fold, l_f will be rather independent of the applied boundary condition (clamped or as here a localised imperfection).

From the symbols in Fig. 10 it can be seen that the half folding length is independent of the reference stress σ_0, slightly dependent on whether the material is viscoplastic or follows time-independent J_2-flow theory ($m = 0.05$ or $m = 0$), and significantly dependent on the materials' strain hardening ($n = 10$ or $n = 3$). The dependence of the strain hardening on the buckling behavour is also discussed by Murray and Bilston (1992). The critical half-wave length for the corresponding time-independent case (dashed curves) is found to be significantly larger for all the shells analysed. Furthermore, the sensitivities of the critical half-wave length l_c and that of resulting

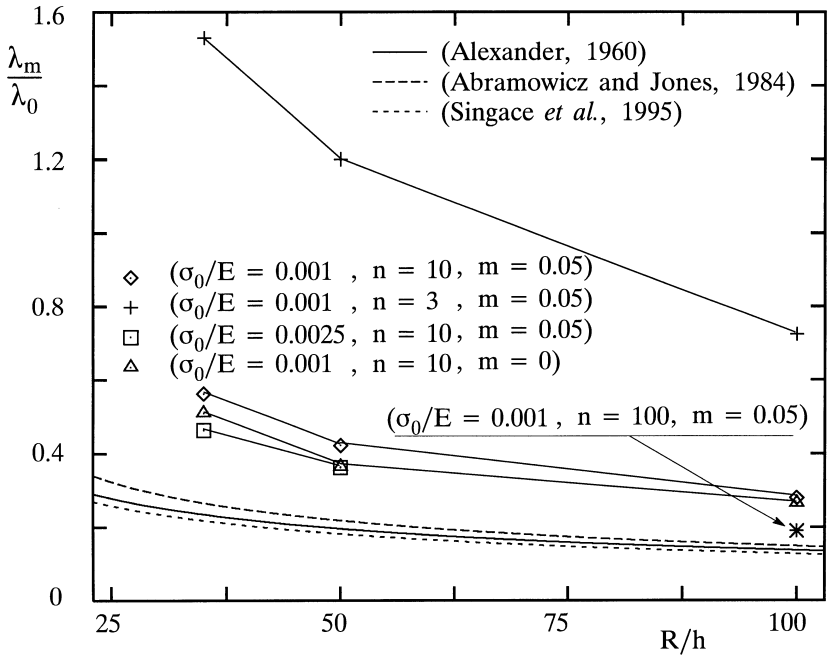

Fig. 11. The mean load in the near periodic region during total structural collapse for different shells compared with approximative mean loads from Alexander (1960), Abramowicz and Jones (1984) and Singace et al. (1995).

folding length l_f to the reference stress σ_0 and strain-hardening exponent n differ. The variation of l_c and l_f with the radius to thickness ratio of the shells is seen to be in good agreement.

The results (solid curves) for the final half-fold length l_f^{Al} (Alexander, 1960), l_f^{AJ} (Abramowicz and Jones, 1984) and l_f^{SER} ($l_f^{SER} \approx l_f^{AJ}$) (Singace et al., 1995) are found to be in reasonable agreement with the half-fold length found in the numerical analyses. Note that these approaches cannot predict the effect of a changed material parameter (σ_0, m or n) on the half folding length ($l_f^{AL}, l_f^{AJ}, l_f^{SER}$). This is due to the fact that these approaches neglect the influence of the elastic strain, the rate hardening ($m \to 0$) and strain hardening ($n \to \infty$) on the collapse mode.

The ability of the approaches (25)–(27) to predict the mean load λ_m in the near periodic region of the shells analysed numerically is presented in Fig. 11. All these approaches are seen to underestimate the mean load significantly. One reason for this is that the plastic deformation of a hardening material (strain hardening or rate-dependence) occurs at a higher stress level than the reference stress σ_0.

It has been suggested that the hardening effect of the material be incorporated in the analytical approaches by replacing the reference stress σ_0 by another more representative stress. Abramowicz and Jones (1984), Grzebieta (1990) and Gupta and Velmurugen (1995) suggest using the ultimate tensile strength as the representative stress, while Wierzbicki (1992) suggests using a stress level corresponding to a strain equal to the average hoop strain. The average hoop strain is estimated from the assumed shape of the collapse fold. Abramowicz and Jones (1984) also used the hoop strain to estimate the average strain rate at which the deformation occurs. This average strain rate is used to estimate the effects of the rate-hardening on the stress level and thereby on the rep-

resentative stress. Note that neither of the above suggestions have any influence on the half-fold length l_f or the shape of the folds.

7. Discussion

The numerical analysis presented, is based on a finite rotation shell theory that accounts for arbitrarily large rotations and deflections of the shell walls. Nevertheless, a small strain theory is assumed to be sufficient for the cases analysed, in spite of the obviously large hoop strains at the outward middle surface of the developed folds. For the shells analysed in Section 6, the maximum loop strain is up to $\varepsilon_{hoop} \approx 0.06$ for $R/h = 100$ and up to $\varepsilon_{hoop} \approx 0.13$ for $R/h = 35$. Rather large strains will also occur away from the middle surface in a small region at the peak of the collapse folds because the folds contain regions with a small radius of curvature of the deformed middle surface r compared with the thickness h of the shell. For $r = 5h$, the strain on the shell surface will be 10%. In addition, when the curvature becomes so large that r/h approaches unity, other finite strain effects set in that are not accounted for in shell theory, as has been explained by Triantafyllidis et al. (1982). The breakdown of the shell theory is most significant for the deformed pattern of the thick-walled shell analysed in Fig. 6(c), where the surface of the shell is no longer well defined by the middle surface and its normal. For the present model, the breakdown of the shell theory in the final stage of each folding results in the prediction of a penetration of the shell surface into itself on the inside of each fold. The reason why the analysis is still considered sufficiently accurate is that both the large strains and the small radius of curvature appear late during the formation of each fold, just before contact. Therefore, a more precise finite strain description would have little influence on the energy absorption calculated and on the deformation pattern of the shell.

The ability of the numerical finite element analysis to model the total structural collapse of a thick-walled shell (concertina collapse mode) has been demonstrated. Both with respect to the initial buckling mode (initial load peak), the following formation of a collapse fold near the boundary, and the progressive near periodic and boundary-insensitive collapse folds. The development of one collapse fold is shown to give two load peaks on the load vs. shortening curve due to the progressive inward and outward buckling.

8. Conclusion

Numerical analyses have been carried out for the axisymmetric collapse of circular cylindrical shells under axial compression. These quasi-static analyses are based on full non-linear shell theory accounting for arbitrarily large rotations of the shell wall. To describe contact between shell walls as the shell folds up, it has been necessary to formulate a contact algorithm. The computations have been used to obtain a parametric understanding of the effect of different shell geometries and material descriptions, see Table 1.

The full numerical analysis allows for a detailed study of the effects of strain hardening. It is found that strain hardening increases the stress level and the energy absorption, as expected. In addition, strain hardening also changes the number and width of the folds.

The material behaviour is described by either time-dependent elasto-viscoplasticity or time-

Table 1
Cases for the dependence of the collapse behaviour on a change in the material and geometrical parameters. The cases are analysed in the figure numbers shown in the brackets

Change of:	Resulting changbe (%) of: Load peak λ_{max}/λ_0 (%)	Mean load $\lambda_m\lambda_0$ (%)	Half folding length l_f/R (%)	Axial length of one fold L_d/R (%)
Radius thickness ratio				
from $R/h = 100$ (Fig. 6(a))	17	103	62	−49
to $R/h = 35$ (Fig. 6(c))		(91 → 112)[a]	(40 → 64)[b]	
Strain hardening exponent				
from $n = 10$ (Fig. 6(b))	95	177	24	50
to $n = 3$ (Fig. 9(a))		(158 → 185)[a]	(23 → 25)[c]	
Rate hardening exponent				
from $m = 0.05$ (Fig. 4)	−7	−9	−7	−11
to $m = 0$ (Fig. 5)		(−14 → −5)[a]	(−7 → −5)[b]	
Reference stress				
from $\sigma_0/E = 0.001$ (Fig. 6(b))	−14	−14	No influence	No influence
to $\sigma_0/E = 0.0025$ (Fig. 9(b))		(−18 → −14)[a]		(<4)
Prescribed shortening rate				
from $\dot{\varepsilon}_a = \dot{\varepsilon}_0/10$ (Fig. 7(a))	25	24[c]	No influence	No influence
to $\dot{\varepsilon}_a = 10\dot{\varepsilon}_0$ (Fig. 7(b))				
Initial localized imperfection				
from $\bar{\bar{\xi}} = 0.1$ (Fig. 8(a))	−35	No influence	No influence	No influence
to $\bar{\bar{\xi}} = 1.0$ (Fig. 8(b))		(<2)		

[a] For the cases in Fig. 11.
[b] For the cases in Fig. 10.
[c] Including initial buckling.

independent J_2-flow theory. For the time-dependent material, an increased deformation rate is found to give a higher stress level and a higher energy absorption for the shell. On the other hand, no changes are found in the corresponding collapse mode (number and width of folds, etc.). When different levels of strain-rate hardening are compared, including the limit of the time-independent case, the viscoplastic material description is observed to influence both the stress level, the energy absorption and the collapse mode.

Furthermore, a possibility to decrease the initial load peak and thereby increase the usefulness of the shell as a shock-absorbing device is demonstrated. This is done without any notable change in the energy absorption of the shells by incorporating a large localised initial imperfection.

Acknowledgements

The author wishes to thank Professor V. Tvergaard at the Technical University of Denmark for many invaluable discussions during the course of this work.

Appendix : incremental variables

The kinematic variable in incremental form is given by Ding (1989) and Başar and Ding (1990). Variable which is linear in v_i is given as

$$\begin{aligned}
\bar{\phi}_{\alpha\beta} &= \phi_{\alpha\beta} + \overset{+}{\phi}_{\alpha\beta}; \quad \overset{+}{\phi}_{\alpha\beta} = \overset{+}{v}_{\beta|\alpha} - \overset{+}{v}_3 \mathring{b}_{\beta\alpha} \\
\bar{\phi}_{\beta 3} &= \phi_{\beta 3} + \overset{+}{\phi}_{\beta 3}; \quad \overset{+}{\phi}_{\beta 3} = \overset{+}{v}_{3|\beta} + \overset{+}{v}_\lambda \mathring{b}^\lambda_\varrho
\end{aligned} \tag{A1}$$

while variable which is nonlinear is given as

$$\bar{\alpha}_{\alpha\beta} = \alpha_{\alpha\beta} + \overset{+}{\alpha}_{\alpha\beta} + \tfrac{1}{2}\overset{++}{\alpha}_{\alpha\beta} \tag{A2}$$

with

$$\overset{+}{\alpha}_{\alpha\beta} = \tfrac{1}{2}(\overset{+}{\phi}_{\beta\alpha} + \overset{+}{\phi}_{\alpha\beta} + \overset{+}{\phi}_{\alpha\lambda}\phi^\lambda_\beta + \phi_{\alpha\lambda}\overset{+}{\phi}^\lambda_\beta + \phi_{\alpha 3}\overset{+}{\phi}_{\beta 3} + \overset{+}{\phi}_{\alpha 3}\phi_{\beta 3}) \tag{A3}$$

$$\overset{++}{\alpha}_{\alpha\beta} = \overset{+}{\phi}_{\alpha\lambda}\overset{+}{\phi}^\lambda_\beta + \overset{+}{\phi}_{\alpha 3}\overset{+}{\phi}_{\beta 3} \tag{A4}$$

and as

$$\bar{\omega}_{\alpha\beta} = \omega_{\alpha\beta} + \overset{+}{\omega}_{\alpha\beta} + \tfrac{1}{2}\overset{++}{\omega}_{\alpha\beta} + \cdots \tag{A5}$$

with

$$\begin{aligned}
\overset{+}{\omega}_{\alpha\beta} = -[&(1+w_3)(\overset{+}{\phi}_{\alpha 3|\beta} + \mathring{b}^\varrho_\beta \overset{+}{\phi}_{\alpha\varrho}) + w_\varrho(\overset{+}{\phi}^\varrho_{\alpha|\beta} - \mathring{b}^\varrho_\beta \overset{+}{\phi}_{\alpha 3}) \\
&+ (\mathring{b}_{\alpha\beta} + \phi_{\alpha 3|\beta} + \mathring{b}^\varrho_\beta \phi_{\alpha\varrho})\overset{+}{w}_3 + (\phi^\varrho_{\alpha|\beta} - \mathring{b}^\varrho_\beta \phi_{\alpha 3})\overset{+}{w}_\varrho]
\end{aligned} \tag{A6}$$

$$\begin{aligned}
\overset{++}{\omega}_{\alpha\beta} = -2\Bigg[&\overset{+}{w}_3(\overset{+}{\phi}_{\alpha 3|\beta} + \mathring{b}^\varrho_\beta \overset{+}{\phi}_{\alpha\varrho}) + \overset{+}{w}_\varrho(\overset{+}{\phi}^\varrho_{\alpha|\beta} - \mathring{b}^\varrho_\beta \overset{+}{\phi}_{\alpha 3}) \\
&+ (\mathring{b}_{\alpha\beta} + \phi_{\alpha 3|\beta} + \mathring{b}^\varrho_\beta \phi_{\alpha\varrho})\frac{\overset{++}{w}_3}{2} + (\phi^\varrho_{\alpha|\beta} - \mathring{b}^\varrho_\beta \phi_{\alpha 3})\frac{\overset{++}{w}_\varrho}{2}\Bigg]
\end{aligned} \tag{A7}$$

The difference vector in incremental form is given by

$$\bar{w}_\varrho = w_\varrho + \overset{+}{w}_\varrho + \tfrac{1}{2}\overset{++}{w}_\varrho + \cdots \tag{A8}$$

with

$$\begin{aligned}
\overset{+}{w}_\varrho l^\varrho_\alpha &= -[\overset{+}{\phi}^\varrho_\alpha w_\varrho + \overset{+}{\phi}_{\alpha 3}(1+w_3)] \\
\overset{+}{w}_3(1+w_3) &= -\overset{+}{w}_\alpha w^\alpha \\
\overset{++}{w}_\varrho l^\varrho_\alpha &= -(\overset{+}{w}_\varrho \overset{+}{l}^\varrho_\alpha + \overset{+}{\phi}^\varrho_\alpha \overset{+}{w}_\varrho + \overset{+}{w}_3 \overset{+}{\phi}_{\alpha 3})
\end{aligned} \tag{A9}$$

$$\overset{+}{w}{}^{+}{}_{3}(1+w_3) = -(\overset{+}{w}_3\overset{+}{w}_3+\overset{+}{w}_\alpha\overset{+}{w}{}^\alpha+\overset{+}{w}{}^{+}{}_\alpha w^\alpha) \tag{A10}$$

where

$$l^\varrho_\alpha = \delta^\varrho_\alpha+\phi^\varrho_\alpha-\frac{w^\varrho}{1+w_3}\phi_{\alpha 3} \tag{A11}$$

$$\overset{+}{l}{}^\varrho_\alpha = \overset{+}{\phi}{}^\varrho_\alpha-\frac{(1+w_3)\overset{+}{w}{}^\varrho-\overset{+}{w}_3 w^\varrho}{(1+w_3)^2}\phi_{\alpha 3}-\frac{w^\varrho}{1+w_3}\overset{+}{\phi}_{\alpha 3} \tag{A12}$$

The incremental membrane stress tensor $\overset{+}{N}$ and the incremental moment tensor $\overset{+}{M}$ are given by

$$\begin{aligned}\overset{+}{N}{}^{\alpha\beta} &= H^{\alpha\beta\gamma\delta}_{(1)}\overset{+}{\alpha}_{\alpha\beta}+H^{\alpha\beta\gamma\delta}_{(2)}\overset{+}{\omega}_{\alpha\beta}+\overset{+}{N}{}^{\alpha\beta}_{*}\\ \overset{+}{M}{}^{\alpha\beta} &= H^{\alpha\beta\gamma\delta}_{(2)}\overset{+}{\alpha}_{\alpha\beta}+H^{\alpha\beta\gamma\delta}_{(3)}\overset{+}{\omega}_{\alpha\beta}+\overset{+}{M}{}^{\alpha\beta}_{*}\end{aligned} \tag{A13}$$

where

$$H^{\alpha\beta\gamma\delta}_{(i)} = \int_{-(h/2)}^{h/2}\hat{\mathscr{L}}^{\alpha\beta\gamma\delta}(\Theta^3)^{(i-1)}\,\mathrm{d}\Theta^3 \tag{A14}$$

$$\overset{+}{N}{}^{\alpha\beta}_{*} = \Delta t\int_{-(h/2)}^{h/2}\dot{\hat{\sigma}}^{\alpha\beta}_{*}\,\mathrm{d}\Theta^3,\quad \overset{+}{M}{}^{\alpha\beta}_{*} = \Delta t\int_{-(h/2)}^{h/2}\dot{\hat{\sigma}}^{\alpha\beta}_{*}\Theta^3\,\mathrm{d}\Theta^3 \tag{A15}$$

References

Abramowicz, W., Jones, N., 1984. Dynamic axial crushing of circular tubes. Int. J. Impact Engng 2, 263–281.

Alexander, J.M., 1960. An approximate analysis of the collapse of thin cylindrical shells under axial loading. Quarterly Journal of Mechanics and Applied Mathematics 13, 10–15.

Allan, T., 1968. Experimental and analytical investigation of the behaviour of cylindrical tubes subject to axial compressive forces. J. Mech. Engng Sci. 10, 182–197.

Andrews, K.R.F., England, G.L., Ghani, E., 1983. Classification of the axial collapse of cylindrical tubes under quasi-static loading. Int. J. Mech. Sci. 25, 687–696.

Başar, Y., 1987. A consistent theory of geometrically non-linear shells with an independent rotation vector. International Journal of Solids and Structures 23, 1401–1415.

Başar, Y., Ding, Y., 1990 Finite-rotation elements for the non-linear analysis of thin shell structures. International Journal of Solids and Structures 26, 83–97.

Başar, Y., Krätzig, W.B., 1989. A consistent shell theory for finite deformation. Acta Mechanica 76, 73–87.

Başar, Y., Krätzig, W.B., 990. Introduction into finite-rotation shell theories and their operator formulation. In Computational Mechanics of Nonlinear Response of Shells, ed. W. B. Krätzig and E. Oñate, pp. 3–30.

Batterman, S.C., 1965. Plastic buckling of axially compressed cylindrical shells. AIAA Journal 3, 316–325.

Benson, J.D.,Hallquist, J.O., 1990. A single surface contact algorithm for the post-buckling analysis of shell structures. Comput. Methods Appl. Mech. Eng. 78, 141–163.

Berstad, T., Langseth, M., Hopperstad, O.S., 1995. Crashworthiness of thin walled aluminium extrusions. In Computational Plasticity—Fundamentals and Applications, ed. D. R. J. Owen and E. Onate, pp. 1901–1912. Pineridge Press, Swansea, U.K.

Ding, Y., 1989. Finite-rotation-elemente zur geometrisce nichtlinearen analyse allgemiener flächentragwerke. Dissertation am Institute für statik und dynamik, Institut für Konstruktiven ingenieurbau, Ruhr-universität in Bochum, Mitteilung Nr. 89-6, F.R.G.

Grzebieta, R.H., 1990. An alternative method for determining the behaviour of round stocky tubes subjected to an axial crush load. Thin Walled Structures 9, 61–89.

Gupta, N.K., Velmurugan, R., 1995. An analysis of Axi-symmetric axial collapse of round tubes. Thin Walled Structures 14, 261–274.

Horton, W.H., Bailey, S.C., Edwards, A.M., 1966. Nonsymmetric buckle patterns in progressive plastic buckling. Experimental Mech. 23, 433–444.

Hutchinson, J.W., Budiansky, B., 1966. Dynamic buckling estimates. AIAA Journal 4, 525–530.

Hutchinson, J.W., Neale, K.W., 1977. Influence of strain-rate sensitivity on necking under uniaxial tension. Acta Metallica 25, 839–846.

Johnson, W., Soden, P.D., Al-Hassani, S.T.S., 1977. Inextensional collapse of thin walled tubes under axial compression. Journal of Strain Analysis 12, 317–330.

Krempl, E., Kallianpur, V.V., 1984. Some critical uniaxial experiments for viscoplasticity at room temperature. Journal of the Mechanics and Physics of Solids 32, 301–314.

Mikkelsen, L.P. 1993. On the analysis of viscoplastic buckling. International Journal of Solids and Structures 30, 1461–1472.

Mikkelsen, L.P., 1995. Elastic-viscoplastic buckling of circular cylindrical shells under axial compression. Eur. J. Mech. A/Solids 14, 901–920.

Murray, N.W., Bilston, P., 1992. Local buckling of thin walled pipes being bent in the plastic range. Thin Walled Structures 14, 411–434.

Niordson, F.I., 1985. Shell Theory. North-Holland Series in Applied Mathematics and Mechanics, Vol. 29. Elsevier science publishers B. V., Amsterdam.

Obrecht, H., 1977. Creep buckling and postbuckling of circular cylindrical shells under axial compression. International Journal of Solids and Structures 13, 337–355.

Peirce, D., Shih, C.F., Needleman, A., 1984. A tangent modulus method for rate dependent solids. Computers and Structures 18, 875–887.

Rice, J.R., 1970. On the structure of stress–strain relations for time-dependent plastic deformation in metals. Journal of Applied Mechanics 37, 728–737.

Singace, A.A., Elsobky, H., 1996. Further experimental investigation on the eccentricity factor in the progressive crushing of tubes. International Journal of Solids and Structures 33, 3517–3538.

Singace, A.A., Elsobky, H., Reddy, T.Y., 1995. On the eccentricity factor in the progressive crushing of tubes. International Journal of Solids and Structures 32, 3589–3602.

Triantafyllidis, N., Needleman, A., Tvergaard, V., 1982. On the development of shear bands in pure bending. International Journal of Solids and Structures 18, 121–138.

Tvergaard, V., 1983a. Plastic buckling of axially compressed circular cylindrical shells. Thin Walled Structures 1, 139–163.

Tvergaard, V., 1983b. On the transition from a diamond mode to an axisymmetric mode of collapse in cylindrical shells. International Journal of Solids and Structures 19, 845–856.

Tvergaard, V., 1985. Rate-sensitivity in elastic–plastic panel buckling. In Aspects of the Analysis of Plane Structures, A Volume in Honour of W. H. Wittrick, ed. D. J. Dawe, R. W. Horsington, A. G. Kamtekar and G. H. Little, pp. 293–308. Clarendon Press, Oxford.

Wierzbicki, T., Bhat, S. U., Abramowicz, W., Brodkin, D., 1992. Alexander revisited—a two folding elements model of progressive crushing of tubes. International Journal of Solids and Structures 29, 3269–3288.